Ocean Modelling 101 (2016) 121–132

Contents lists available at ScienceDirect

Ocean Modelling

journal homepage: www.elsevier.com/locate/ocemod

ENDLESS: An extended nonperiodic domain large-eddy simulation approach for scalar plumes

Bicheng Chen[a], Di Yang[b], Charles Meneveau[c], Marcelo Chamecki[a,*]

[a] Department of Meteorology, Pennsylvania State University, University Park, Pennsylvania
[b] Department of Mechanical Engineering, University of Houston, Houston, Texas
[c] Department of Mechanical Engineering, Johns Hopkins University, Baltimore, Maryland

ARTICLE INFO

Article history:
Received 25 August 2015
Revised 16 February 2016
Accepted 8 April 2016
Available online 9 April 2016

MSC:
00-01
99-00

Keywords:
ENDLESS
Scalar transport
Large domain
Ocean mixed layer
Langmuir circulation
Oil plume

ABSTRACT

Large-eddy simulation (LES) has proven to be a valuable tool for high-fidelity modeling of environmental and geophysical turbulent flows. An important application of LES is to study the transport of effluents (e.g. oils from a subsea blowout) in the ocean mixed layer (OML). Oil plumes being transported in the OML experience the action of shear-generated turbulence, Langmuir circulations, Ekman transport and submesoscale quasi-geostrophic eddies. To resolve such turbulent processes, grid sizes of a few meters are desirable while horizontal domain sizes of LES are typically restricted from hundreds of meters to a few kilometers, for LES to remain practically affordable. Yet transported oil plumes evolve to large scales extending to tens or even hundreds of kilometers. In this study, the Extended Nonperiodic Domain LES for Scalar transport (ENDLESS) is proposed as a multi-scale approach to tackle this challenge while being computationally affordable. The basic idea is to simulate the shear turbulence and Langmuir circulations on a small horizontal domain with periodic boundary conditions while the resulting transport velocity field is replicated periodically following adaptively the large-scale plume as it evolves spatially towards much larger scales. This approach also permits the superposition of larger-scale quasi two-dimensional flow motions on the oil advection, allowing for coupling with regional circulation models. A validation case and two sample applications to oil plume evolution in the OML are presented in order to demonstrate key features and computational speedup associated with the ENDLESS method.

1. Introduction

Transport and dilution of effluents by turbulent motion of fluids is one of the most fundamental aspects of environmental systems (Imberger, 2013). When exploring the complex nature of environmental flows, progress in understanding turbulent plumes has benefited greatly from the use of numerical simulations to complement observational data. High fidelity numerical simulations of these flows are now possible using the large-eddy simulation (LES) technique (e.g. Moeng, 1984; McWilliams et al., 1997; Chamecki et al., 2009; Grant and Belcher, 2009). With current computational power, it is already possible to simulate large spatial domains with resolution fine enough to capture the dynamical interactions of eddies that contain most of the turbulent kinetic energy. As an example, LES of the atmospheric boundary layer and the ocean mixed layer can be performed on domains of several kilometers with grid sizes of a few meters (Sullivan and Patton, 2011; Özgökmen et al., 2011; Hamlington et al., 2014). Such highly resolved simulations provide great levels of detail that are invaluable for studying structure and statistical properties of effluent plumes (hereafter referred to as "scalar" plumes).

When studying the spatial structure of a scalar plume, one is typically interested in characterizing the growth of the plume and associated concentration dilution. In the case of growing plumes originated from localized sources, the large-scale flow typically transports the plume over a distance that is much larger than the sizes of the energy containing turbulent eddies. These flows, in which the spatial distance over which the scalar plume develops is much larger than the largest scales of the three-dimensional turbulence, are the focus of this paper. A highly relevant example that has gained renewed interest in the wake of the Deepwater Horizon accident in the Gulf of Mexico in 2010 is the transport of oil plumes in the ocean mixed layer (OML). In this case, mean currents and submeso- and mesoscale eddies transport oil plumes over several kilometers within the timescales of turbulent mixing.

* Corresponding author. Tel.: +(814) 863-3920; fax: +(814) 865-3663.
E-mail address: chamecki@psu.edu (M. Chamecki).

http://dx.doi.org/10.1016/j.ocemod.2016.04.003
1463-5003/

Numerical simulations of oil transport are typically performed using regional or global ocean models (e.g. Le Henaff et al., 2012; Huntley et al., 2013). These models are capable of reproducing most of the large-scale flow features, but rely on highly simplified parameterization of the effects of turbulence and other processes within the OML. A widely used approach to represent these effects is the K-Profile Parameterization (KPP) (Large et al., 1994). However, the complex flow field in the OML, originated from the interactions of wind-stress forcing, surface waves, and Coriolis effects, gives rise to a wide variety of patterns in surface oil plumes (Yang et al., 2014). In particular, Langmuir circulations generated by the interactions of surface waves and wind-driven currents play an important role in the near-surface dynamics (Langmuir, 1938; Leibovich, 1983; Thorpe, 2004). The presence of Langmuir circulations modulates turbulence in the OML, greatly enhancing vertical mixing of tracers. On the other hand, buoyant particles become trapped in the surface convergence zones produced by Langmuir cells and are organized in fingers that provide a visual signature of these flow structures (e.g. McWilliams et al., 1997; McWilliams and Sullivan, 2000; Sullivan and McWilliams, 2010; Van Roekel et al., 2012). Because oil transport depends strongly on the small-scale physics of the OML and the specific details of Langmuir circulations near the ocean surface, simulations using the coarse resolutions of regional models may inherently miss important detailed physics. Despite the existing efforts in improving KPP (e.g., see McWilliams and Sullivan, 2000; Smyth et al., 2002; Yang et al., 2015), a multiscale approach that combines the capabilities of regional models in reproducing submeso- and mesoscale motions and the high-fidelity fine-scale turbulence produced by LES is desirable. The major advantage of using LES to study the OML is that LES can resolve Langmuir circulations and capture their dynamical coupling with turbulence explicitly, producing results in good agreement with observations (Scotti, 2010).

The spacing of the convergence zones of Langmuir turbulence ranges from a few to hundreds of meters (Leibovich, 1983), imposing restrictions on the horizontal grid spacing of the LES. To keep the computational cost reasonable, many studies (McWilliams et al., 1997, 2014; Van Roekel et al., 2012; Sullivan et al., 2012; Yang et al., 2014, 2015) restricted their total horizontal domain size to be at most a few kilometers. Even though this is enough to capture the dynamics of Langmuir turbulence, in most cases it is the bare minimum to capture the development of surface oil plumes (Yang et al., 2015). If one is interested in the longer time evolution of oil droplet plumes as they extend and grow to larger scales, such domains are too small. Furthermore, since droplets of different sizes are typically transported in different mean directions due to the interplay of buoyancy, Ekman transport and Langmuir circulations (Yang et al., 2015), plumes containing a range of droplet sizes can cover regions of complicated shapes, with sizes much larger than a few kilometers. Even though very large simulations resolving Langmuir cells on domains of about 20 × 20 km are now possible, they require immense computational resources (Hamlington et al., 2014), and it is impractical to perform enough simulations to map a large parameter space covering a wide range of oil droplet sizes and wind and wave conditions. Thus, oil dispersion in the OML is one of the typical problems in which the domain size required to study the plume transport is much larger than the one required to represent the dominant dynamical features (here assumed to be Langmuir circulations, surface waves, and turbulence).

To avoid the high computational cost of enlarging the simulation domain to capture the growth of the scalar plume, a new approach called the Extended Nonperiodic Domain LES for Scalar transport (ENDLESS) is developed. The approach is based on the observation that the vast majority of computational cost of a regular LES simulation is associated with the evolution of the velocity and pressure fields. The basic idea is to simulate the flow field in a horizontally small domain (hereafter termed "velocity-field LES domain") designed to capture the relevant flow dynamics. Simultaneously, the scalar field evolution is simulated over an effectively large domain, referred to as the "extended domain", and designed to capture the desired growth of the scalar plume. This is made possible by leveraging the use of periodic boundary conditions in the flow solver.

In the ENDLESS framework, the effects of larger scale flow features (such as submeso- and mesoscale eddies simulated by a regional model) are introduced by assuming scale separation and superposition of a prescribed velocity field to the LES resolved velocity in the scalar advection equation. Because ENDLESS has a relatively low computational cost, it is feasible to use it together with a regional model in practical applications to oil dispersion predictions. More specifically, ENDLESS can be used in a subregion of interest within the regional model domain (e.g. a region where an oil plume is present) to "downscale" the velocity field, leading to more accurate predictions of local oil transport. Moreover, by adaptively determining the required extended domain for scalar, an ENDLESS simulation can track the evolution of the plume within the larger domain of the regional model for a very long time with affordable computational cost. It is important to point out that the inherent assumption of scale separation (between mesoscale motions from regional models and 3D turbulent eddies from LES) is an approximation that may not hold exactly in practice (see e.g. Özgökmen et al., 2012; Hamlington et al., 2014). Still, ENDLESS is expected to provide predictions that are more accurate and rich in details than what can be obtained using only a regional model without including any smaller-scale information.

Finally, we remark that the idea of periodic replication of LES velocity fields to advect scalar fields has been independently introduced recently in the context of scalar plumes in the atmospheric boundary layer (Matheou and Bowman, 2015). The present paper significantly extends that idea by (i) including real-time spatial adaptivity of the simulation domain, (ii) proposing a strategy for coupling the framework with regional models at larger scales, and (iii) implementing the method to model transport in the upper ocean.

This paper is organized as follows. The ENDLESS approach is described in Section 2 while the application to oil dispersion is detailed in Section 3. Results are provided in Section 4 and conclusions are presented in Section 5.

2. Extended nonperiodic domain LES for scalars in the OML

In LES of the ocean mixed layer, one solves the filtered Navier–Stokes and temperature transport equations

$$\nabla \cdot \widetilde{\mathbf{u}} = 0 \; ; \tag{1}$$

$$\frac{\partial \widetilde{\mathbf{u}}}{\partial t} + \widetilde{\mathbf{u}} \cdot \nabla \widetilde{\mathbf{u}} = -\frac{1}{\rho_0} \nabla \widetilde{p} + \nu \nabla^2 \widetilde{\mathbf{u}} - \nabla \cdot \boldsymbol{\tau} + \widetilde{\mathbf{u}} \times f_c \mathbf{e}_z + (1 - \frac{\widetilde{\rho}}{\rho_0}) g \mathbf{e}_z + \widetilde{\mathbf{f}} \tag{2}$$

$$\frac{\partial \widetilde{\theta}}{\partial t} + \nabla \cdot (\widetilde{\mathbf{u}}_\theta \widetilde{\theta}) = D_\theta \nabla^2 \widetilde{\theta} - \nabla \cdot \boldsymbol{\pi}_\theta, \quad \tilde{\rho} = \rho_0 [1 - \alpha_\theta (\tilde{\theta} - \theta_0)] \tag{3}$$

on a coarse discrete numerical grid (coarse with respect to the smallest scale of fluid motion, the Kolmogorov scale). Here a tilde denotes a variable resolved by the LES grid, $\mathbf{u} = (u, v, w)$ is the Eulerian velocity vector with u, v and w being the components in x, y and z directions, respectively, p is a modified pressure, ρ_0 is the reference density, ν is the fluid kinematic viscosity, $\boldsymbol{\tau} = (\widetilde{\mathbf{u}\mathbf{u}} - \widetilde{\mathbf{u}}\widetilde{\mathbf{u}})$ is the subgrid-scale (SGS) stress tensor and $\mathbf{f}$ accounts for possible additional forcing terms that are specific to each application

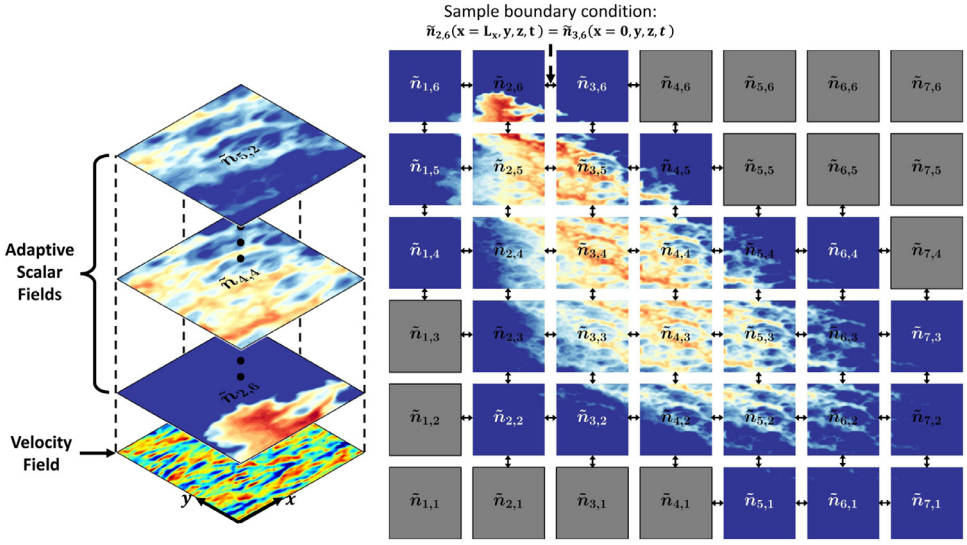

Fig. 1. ENDLESS approach application to simulate oil dispersion in the ocean mixed layer. Here $\chi = n$ is used to represent oil mass concentration $n(\mathbf{x}, t)$. The left panel illustrates how several scalar fields (representing filtered mass concentration, $\tilde{n}_{I,J}$, of oil droplets within domain indexed by (I, J)) are all advected by the same velocity field. The right panel illustrates how the information from the different scalar fields can be assembled to form the extended domain. The colors indicate surface concentration of oil droplets. The grey patches represent scalar fields not being used in the current time step with the adaptive technique. (For interpretation of the references to colour in this figure legend, the reader is referred to the web version of this article.)

(as an example, $\mathbf{f}$ could account for the Stokes drift due to cumulative effects of surface waves, see Section 3.1). Also, f_c is the Coriolis parameter, g is the gravitational acceleration, $\mathbf{e}_z$ is the unit vector in the vertical direction. Furthermore, density ρ is specified as a function of temperature θ as shown in Eq. (3), where $\alpha_\theta = 2 \times 10^{-4}\,\mathrm{K}^{-1}$ is the thermal expansion rate for the sea water (McWilliams et al., 1997), and ρ_0 and θ_0 are the reference density and temperature, respectively. The density field ρ is evaluated from the temperature field θ, which is evolved using the advection–diffusion equation in (3). In Eq. (3), $\tilde{\mathbf{u}}_\theta$ is the resolved temperature advection velocity, D_θ is the thermal diffusivity, and $\boldsymbol{\pi}_\theta = (\widetilde{\mathbf{u}\theta} - \tilde{\mathbf{u}}\tilde{\theta})$ represents the SGS heat flux.

Now, we consider transport of a scalar quantity χ such as an oil concentration field. It is evolved by solving an additional filtered advection–diffusion equation

$$\frac{\partial \tilde{\chi}}{\partial t} + \nabla \cdot \left[\left(\tilde{\mathbf{u}}_\chi + \mathbf{U}_{\mathrm{LS}} \right) \tilde{\chi} \right] = D \nabla^2 \tilde{\chi} - \nabla \cdot \boldsymbol{\pi}_\chi + Q_\chi . \tag{4}$$

Here, $\tilde{\mathbf{u}}_\chi$ is the resolved advection velocity for the scalar field, $\mathbf{U}_{\mathrm{LS}}$ is a two-dimensional large-scale velocity (discussed further below), D is the scalar diffusivity, and Q_χ is a source term representing the release of a scalar from a localized source. In addition, $\boldsymbol{\pi}_\chi = (\widetilde{\mathbf{u}\chi} - \tilde{\mathbf{u}}\tilde{\chi})$ is the SGS scalar flux, which must be parameterized along with the SGS momentum and heat fluxes. The scalar advection velocity $\tilde{\mathbf{u}}_\chi$ can include the droplet–fluid relative velocity. In applications to the OML described in the next section, $\tilde{\mathbf{u}}_\chi$ (and $\tilde{\mathbf{u}}_\theta$) also includes effects of Stokes drift. Moreover, $\mathbf{U}_{\mathrm{LS}}$ represents the effects of large-scale flow features (not present in the velocity field produced by the LES) on scalar transport, and will be discussed in more detail at the end of this section.

The numerical implementation of the code used here is presented in the next sections. For now it is sufficient to point out that, as in a large number of simulations of turbulent environmental flows such as those in the atmospheric boundary layer (Moeng, 1984; Henn and Sykes, 1992; Tseng et al., 2006; Chamecki et al., 2009) and the ocean mixed layer (McWilliams et al., 1997; Yang et al., 2014; Hamlington et al., 2014), boundary conditions for the velocity, pressure and temperature fields in the horizontal directions are periodic (this is usually done as a way to avoid the requirement of specifying artificial inflow conditions, as well as to facilitate the use of spectral methods to accurately resolve turbulence motions over a wide range of scales).

The first (conceptual) step in the proposed ENDLESS approach is the periodic extension of the velocity fields computed from LES. Due to the use of periodic boundary conditions, if the velocity and pressure fields are "extended" in horizontal directions by replicating the original domain many times, these extended velocity and pressure fields also satisfy the mass and momentum conservation Eqs. (1) and (2). In practice, however, simply replicating the velocity field onto a very large domain and solving the scalar equation on an actual horizontally extended domain would be quite cumbersome since different numbers of grid points and domain sizes for the velocity and scalar solvers would be involved. And, as it will be shown below, additional computational cost would be incurred because of the inability to exploit adaptivity. Alternatively, instead of solving a single scalar field $\tilde{\chi}(\mathbf{x}, t)$ for $\mathbf{x}$ extending over the entire large domain where the replicated velocity field resides, the scalar field is represented by $N_p(t)$ separate subset scalar fields $\tilde{\chi}_{I,J}(\mathbf{x}, t)$ with $\mathbf{x}$ defined over only the much smaller "velocity-field LES domain". The number of scalar fields $N_p(t)$ depends on how many "velocity-field LES domains" are required to cover the plume as it evolves in time t. Fig. 1 shows a sketch of the proposed method when the method is applied to a filtered oil droplet concentration field $\chi = n$. The number $N_p(t)$ is the number of small occupied squares in Fig. 1b, while the indices I and J identify each square. If at a given time the plume can be contained in a large rectangular domain of size $M_x L_x$ and $M_y L_y$ then I and J can range between $I = 1, \cdots, M_x$ and $J = 1, \cdots, M_y$, and the total number of squares shown in Fig. 1 (including inactive grey squares and active ones containing scalar field) is given by $M_x M_y$. Each of the N_p domains contains a separate field $\tilde{\chi}_{I,J}(\mathbf{x}, t)$ that is resolved on the LES domain of size $L_x \times L_y \times L_z$. Each of the N_p scalar fields obey continuity boundary conditions so that the union of the N_p domains represents the totality of the plume. Specifically, the following scalar boundary conditions represent continuous exchange of information about scalar concentrations between each neighboring subset scalar fields:

$$\begin{cases} \tilde{\chi}_{I,J}(0, y, z, t) = \tilde{\chi}_{I-1,J}(L_x, y, z, t), \\ \tilde{\chi}_{I,J}(L_x, y, z, t) = \tilde{\chi}_{I+1,J}(0, y, z, t), \\ \tilde{\chi}_{I,J}(x, 0, z, t) = \tilde{\chi}_{I,J-1}(x, L_y, z, t), \\ \tilde{\chi}_{I,J}(x, L_y, z, t) = \tilde{\chi}_{I,J+1}(x, 0, z, t). \end{cases} \tag{5}$$

In practice, for an explicit time integration, the right-hand-side values in equation set (5) are evaluated at the current time-step and the time integration results in the scalar at next time-step (i.e., information at time t is used as boundary condition for time $t + \Delta t$). The extended domain is then assembled from the matrix of subset scalar fields.

In the current framework, the ENDLESS approach is designed to adaptively add and remove scalar fields $\widetilde{\chi}_{I,J}(\mathbf{x}, t)$ based on the realtime evolution of the plume in the simulation. Thus, the ENDLESS domain activates scalar fields in regions where the minimum concentration exceeds some predefined threshold value and deactivates scalar fields that are no longer needed, and $N_p(t)$ evolves in time. In practice, this is achieved by monitoring the concentration both inside and at the edge of a particular domain. If the concentration at the edge exceeds a threshold, a new subset scalar field is added beyond this particular edge where the concentration is detected to be growing. By adopting the adaptive technique, the overall effective domain actively involved in the ENDLESS calculation is dynamically determined by the contour of scalar plume and has the ability to automatically follow the plume. The sample application of ENDLESS to oil dispersion in the OML presented in Fig. 1 shows that the grey areas representing regions without scalar are not being used at the instant depicted because they have no concentrations above the threshold value. Scalar computation within these regions can be activated at any time, as any of the regions in which the scalar is being computed could be deactivated. The boundary conditions at the edges of the extended domain (i.e. the boundaries between colored and grey squares in Fig. 1) are assigned to have zero-value for inlet boundaries and zero-gradient for outlet boundaries.

In the specific application of Eq. (4) to oil transport in the OML, $\mathbf{U}_{\mathrm{LS}}$ can be used to include the effects of submeso- and mesoscale eddies (e.g. Poje et al., 2014) on the transport of oil plumes. In practical applications, $\mathbf{U}_{\mathrm{LS}}$ can be obtained from a regional or global ocean circulation model. One may also use analytical synthetic velocity fields to prescribe $\mathbf{U}_{\mathrm{LS}}$, e.g. for simplified demonstration studies as done in the applications discussed in the next section. We again stress the inherent scale separation assumption made, neglecting possible two-way nonlinear dynamical couplings between $\mathbf{U}_{\mathrm{LS}}$ and the 3D LES velocity field. Clearly, in many cases such interactions can be important. As an example, in the OML, Langmuir turbulence can be significantly modulated by submesoscale eddies (Hamlington et al., 2014). Keeping this limitation in mind, we proceed to apply and demonstrate ENDLESS in the specific context of oil dispersion in the OML and return to the issue of scale separation in Section 5.

3. Application to oil dispersion in the OML

3.1. Numerical model

The typical approach to simulate Langmuir turbulence in the OML using LES is to use the Craik–Leibovich equations (Craik and Leibovich, 1976; Craik, 1977; Leibovich, 1977a; 1977b). These equations consist of a wave-averaged version of the Navier–Stokes equations, which include an additional vortex force term originated from the wave-induced Stokes drift current. In essence, this approach captures the main cumulative effects of surface waves on the ocean turbulence without requiring the explicit representation of the waves (which would in turn require tracking the position of the free surface, finer spatial and temporal resolution, etc.). This simplified approach produces accurate representation of the Langmuir cells using a "flat ocean" surface, corresponding to the averaged ocean surface elevation. Thus, in this specific OML application, the forcing term $\widetilde{\mathbf{f}}$ in Eq. (2) is given by

$$\widetilde{\mathbf{f}} = \mathbf{u}_s \times f_c \mathbf{e}_z + \mathbf{u}_s \times \widetilde{\boldsymbol{\omega}}, \tag{6}$$

representing the Stokes Coriolis force (McWilliams et al., 1997) and the vortex force from the Craik–Leibovich equation, where $\mathbf{u}_s$ is the Stokes drift velocity due to the accumulated effect of the surface gravity waves, and $\boldsymbol{\omega} = \nabla \times \mathbf{u}$ is the fluid vorticity.

Because the wave-induced Stokes drift velocity $\mathbf{u}_s$ also contributes to scalar transport, the advection velocity for the temperature field is set to $\widetilde{\mathbf{u}}_\theta = \widetilde{\mathbf{u}} + \mathbf{u}_s$. Periodic boundary conditions on the horizontal directions are used for velocity and temperature, where the latter field also evolves on the "velocity-field LES domain" since the temperature field is horizontally statistically homogeneous.

A scalar field $\chi = n$ is used to describe the (monodispersed) oil droplet mass concentration field, following the approach introduced by Yang et al. (2014). The advection velocity for the oil droplet mass concentration is given by

$$\widetilde{\mathbf{u}}_n = \widetilde{\mathbf{u}} + \mathbf{u}_s + w_r \mathbf{e}_z + (R-1)\tau_d \frac{\mathrm{D}\widetilde{\mathbf{u}}}{\mathrm{D}t}. \tag{7}$$

Here, $w_r = (\rho_0 - \rho_d) g d^2 / \left(18 \mu_f\right)$ is the rise velocity of oil droplets with effective spherical diameter d and oil density ρ_d, μ_f is the viscosity of water, $R = 3\rho_0/(2\rho_d + \rho_0)$ is the acceleration parameter which includes the added mass effect, $\tau_d = (\rho_d + \rho_0/2) d^2 / \left(18 \mu_f\right)$ is the droplet response time scale (Ferry and Balachandar, 2001), and $\mathrm{D}\widetilde{\mathbf{u}}/\mathrm{D}t = \partial\widetilde{\mathbf{u}}/\partial t + \widetilde{\mathbf{u}} \cdot \nabla \widetilde{\mathbf{u}}$.

Closure of the LES equations requires models for the SGS fluxes of momentum, heat, and droplet mass concentration. In the present sample application of ENDLESS, the SGS stress tensor is modeled using the Smagorinsky model, $\tau_{ij}^d = -2\nu_\tau \widetilde{S}_{ij} = -2(c_s\Delta)^2 |\widetilde{\mathbf{S}}| \widetilde{S}_{ij}$. Here, τ_{ij}^d is the deviatoric part of the stress tensor, $\widetilde{S}_{ij}$ is the resolved strain rate tensor, ν_τ is the SGS eddy viscosity, Δ is the grid (filter) scale of LES, and c_s is the Smagorinsky coefficient (c_s is calculated from the Lagrangian scale-dependent dynamic model (Bou-Zeid et al., 2005)). The SGS heat and scalar concentration fluxes $\boldsymbol{\pi}_\theta$ and $\boldsymbol{\pi}_n$ are parameterized as $\boldsymbol{\pi}_\theta = -(\nu_\tau/\mathrm{Pr}_\tau)\nabla\widetilde{\theta}$ and $\boldsymbol{\pi}_n = -(\nu_\tau/\mathrm{Sc}_\tau)\nabla\widetilde{n}$ with a constant turbulent Prandtl number $\mathrm{Pr}_\tau = 0.4$ and turbulent Schmidt number $\mathrm{Sc}_\tau = 0.8$ (Yang et al., 2014). In addition, in the present application the viscous and molecular diffusion terms are neglected in view of the very large Reynolds and Péclet numbers.

The numerical discretization for momentum and temperature equations combines a pseudo-spectral approach in the horizontal directions and a second-order centered finite-difference scheme in the vertical direction. Periodic boundary conditions are applied in the horizontal directions for the velocity, pressure and temperature fields. The equation for the oil droplet mass concentration is discretized using a finite-volume approach, with the bounded third-order upwind interpolation scheme SMART (Gaskell and Lau, 1988) applied to the advection term. The coupling of the pseudo-spectral approach with the finite-volume discretization follows Chamecki et al. (2008). The second-order Adams–Bashforth scheme is applied for time advancement, combined with a standard projection method to enforce the incompressibility constraint.

3.2. Simulation setup

Results of six simulations are reported in this manuscript. The first two simulations are carried out to test that the LES domain used is sufficiently large to ensure that ENDLESS captures all relevant 3D turbulent motions, while the other four are used as demonstrations of the full features in the ENDLESS approach including adaptive domain and large-scale advection. The key simulation parameters are summarized in Table 1, and a sketch of the simulation configuration is shown in Fig. 2. (Some additional shorter runs are performed to measure computational savings, see Section 4.2.)

In all simulations, the vertical domain has a depth of $L_z = 300\,\mathrm{m}$ with the initial mixed layer extending down to $z_i = 100\,\mathrm{m}$ (be-

Table 1
Simulation parameters.

Parameter (unit)	Symbol	Value
Grid spacing (m)	$dx \times dy \times dz$	$10 \times 10 \times 2$
Time step (s)	dt	0.1
Wind Speed at 10m height (m s^{-1})	U_{10}	10
Friction velocity in water (cm s^{-1})	u_*	1.25
Wave amplitude (m)	a	2.38
Wave length (m)	λ	150
Stoke drift at surface (cm s^{-1})	U_s	15
Coriolis frequency (s^{-1})	f	7×10^{-5}
Turbulent Langmuir number	La_t	0.29
Thermocline depth (m)	z_i	100
Droplet diameter (μm)	d	250, 500
Droplet rise velocity (cm s^{-1})	w_r	0.54, 2.17
Source layer (grid points)	k_{src}	70
Source depth (m)	z_{src}	139
Source mass flow rate (kg s^{-1})	Q_s	1.0
Sea water density (kg m^{-3})	ρ	1031.0
Viscosity of sea water (kg $(ms)^{-1}$)	μ_f	1.08×10^{-3}
Thermal expansion rate of sea water (K^{-1})	α_θ	2×10^{-4}
Oil density (kg m^{-3})	ρ_d	859.9

low which a density gradient $d\rho/dz = -2 \times 10^{-3}\,\mathrm{kg\,m^{-4}}$ is used for the thermocline). The oil is injected from a localized source below the mixed layer (the exact source location for each simulation is specified in Section 4) and the source mass flow rate is $Q_s = 1\,\mathrm{kgs^{-1}}$, following Yang et al. (2014). A constant wind stress $\tau_w = 0.156\,\mathrm{N\,m^{-2}}$ in the x-direction is applied on the ocean surface, corresponding to a wind speed of about $10\,\mathrm{ms^{-1}}$ at 10 m height and a friction velocity in water of $u_* = 0.0125\,\mathrm{ms^{-1}}$. The wave propagation is parallel to the wind stress, and the wave parameters are chosen so that the turbulent Langmuir number (McWilliams et al., 1997) is $La_t = (u_*/U_s)^{1/2} = 0.29$, a typical value from observations (Belcher et al., 2012). Here the Stokes drift velocity is given by $\mathbf{u}_s(z \le 0) = \mathbf{e}_x U_s e^{2kz}$, and $U_s = |\mathbf{u}_s(z=0)| = \sqrt{g\lambda/2\pi}\,(2\pi a/\lambda)^2$ (Yang et al., 2015) is the magnitude of the surface Stokes drift velocity, where a is the wave amplitude, λ is the wavelength, $k = 2\pi/\lambda$ is the wavenumber, and $\mathbf{e}_x$ is the unit vector in the x-direction. In the results reported next, an overbar is used to represent a time average and angle brackets are used to indicate spatial averages over horizontal planes.

4. Results

4.1. Validation simulations

For the first two simulations, the goal is to test the accuracy of using periodic repetitions of LES fields as part of ENDLESS. Both simulations are configured to model the oil plume on a horizontal domain of 1 km × 1 km with identical physical parameters. In particular, in the first simulation, the flow and oil transport are simulated using a standard LES on the full, single domain. In the second simulation, the same oil dispersion problem is simulated using ENDLESS with a smaller 0.5 km × 0.5 km "velocity-field LES domain" and 4 different scalar fields ($M_x = M_y = 2$). The two simulations thus have equivalent effective total domain size and can be compared to validate the basic concept of the ENDLESS method. In both simulations, the location of the oil source is $(x, y, z) = (295, 795, -139)$ m, the effective diameter of oil droplets is $d = 250\,\mu$m, and $\mathbf{U}_{\mathrm{LS}} = 0$ is used to simplify the validation. Data are sampled for statistical analysis after the velocity and oil concentration fields have reached a statistically steady state.

The first critical test of the simulation is to ensure that, for the application and parameter values of the turbulence at hand, a "velocity-field LES domain" of 0.5 × 0.5 km is large enough to appropriately represent the largest eddies in the resolved 3D turbulent flow. This is done by assessing the two-point autocorrelations for each velocity component (Moin and Kim, 1982). Results for u and w are presented in Fig. 3 (results for v are very similar to those for u). The autocorrelations are found to be sufficiently small (absolute values smaller than 0.1) at lags corresponding to half of the domain extent, confirming that the "velocity-field LES domain" is large enough to capture the largest scales in the flow and that the use of periodic boundary conditions will not cause artificial modulation to the flow structures in Langmuir turbulence. In this case, one would expect the statistical properties of the velocity fields in ENDLESS and standard simulations to be indistinguishable (the instantaneous fields are different, as any two distinct realizations of the same statistically steady turbulence flow would appear different in details).

As expected, the mean Eulerian velocity hodograph, the momentum flux hodograph and the vertical velocity variance are very similar for these two simulations (Fig. 4). Note that the turning of the velocity and Reynolds stress vectors typical of the OML (due to Ekman transport) are observed in both simulations, and the enhanced values of the vertical velocity variance characteristic of Langmuir turbulence (e.g. McWilliams et al., 1997; Yang et al., 2015) are well reproduced within the 0.5 km × 0.5 km "velocity-field LES domain" (when compared to the 1 km × 1 km one).

The presence of Langmuir circulations can be observed through the formation of strong and narrow downwelling zones in the vertical velocity fields near the surface. These structures are shown in Figs. 5(a and d), for both the standard and ENDLESS simulations, respectively. The flow patterns are very similar between these two simulations and the orientation and width of the cells are indistinguishable. Oil droplets tend to accumulate in the surface convergence bands right above these downwelling regions, forming "fingered patterns" (Yang et al., 2014), as illustrated in Figs. 5(b and e). The time-averaged surface oil plumes of these two simulations

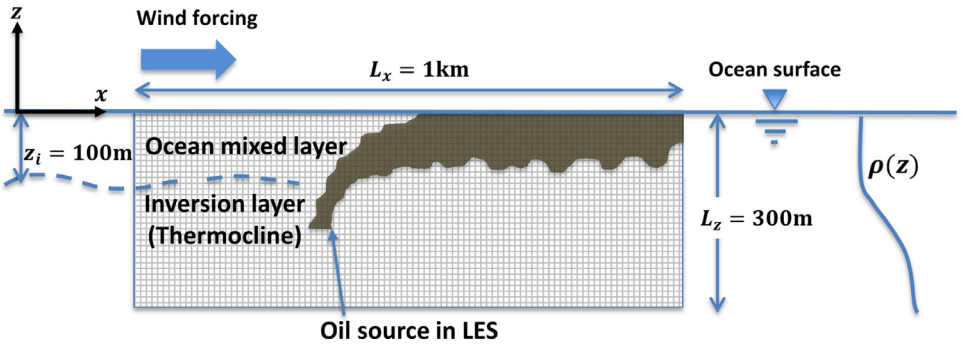

Fig. 2. Domain sketch of the validation experiment. The wind and wave directions are parallel to each other and point in the positive x-direction. The oil is released below the ocean mixed layer.

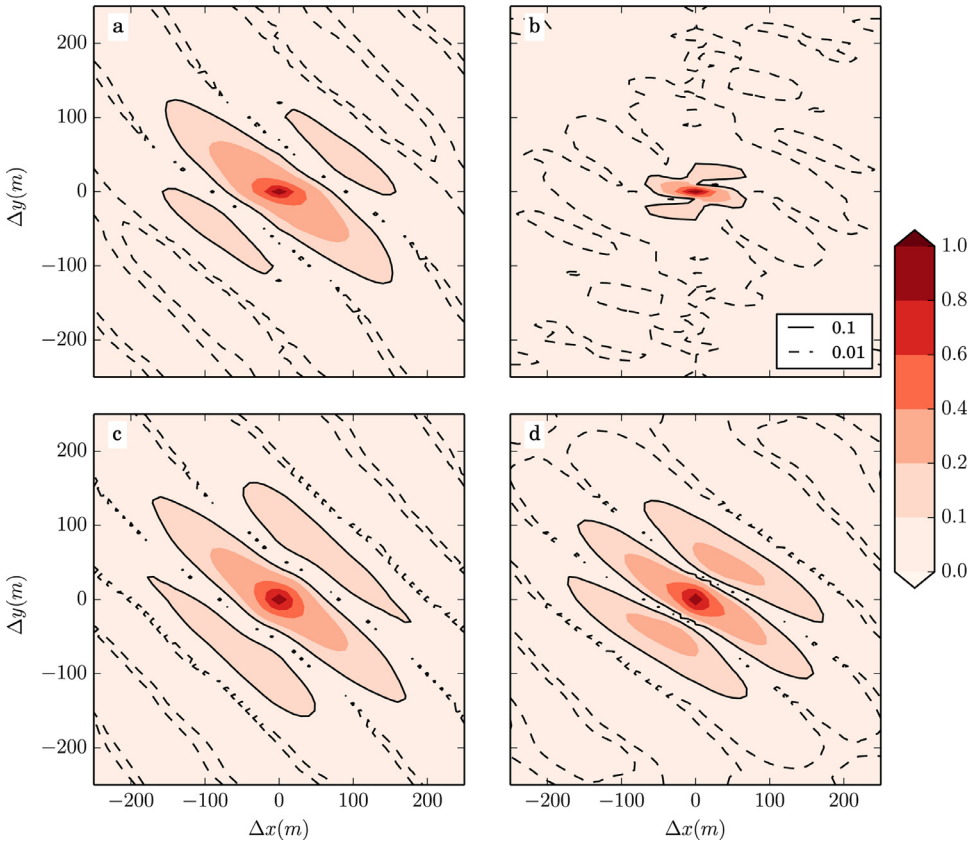

Fig. 3. The 2D two-point spatial autocorrelation function of velocity field: The top row is the result from $z = -10$ m, and the bottom row is the result from $z = -50$ m; (a, c) are the correlations of u-component, (b, d) are the correlations of w-component. Contours are also shown for correlations of 0.1 (solid lines) and 0.01 (dashed lines).

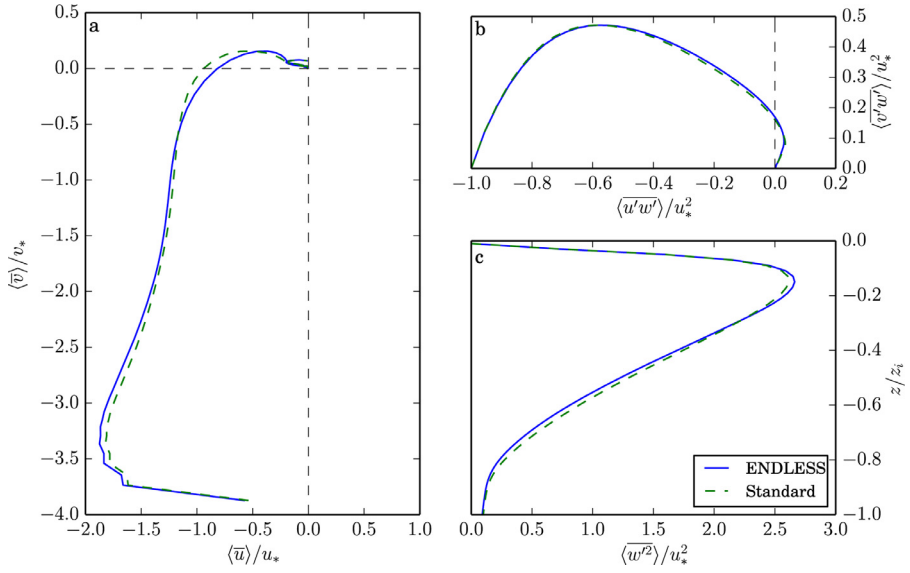

Fig. 4. Hodographs of (a) horizontal Eulerian velocity (without Stokes drift velocity) and (b) turbulent momentum flux, and (c) the profiles of vertical velocity variance.

(Figs. 5c and f) show very good agreement for both the direction of surface plume centerline and the plume growth rate in the downstream direction. Here the deflection of the plume centerline direction with respect to the wind and wave direction (i.e. the x-direction) is generated by the change in flow direction with depth caused by the Coriolis force (i.e. Ekman transport). Finally, probability density functions (PDF) of oil concentration at multiple locations and depths from these two simulations are compared in Fig. 6. The agreement for the plume statistics between these two simulations confirms the validity of the ENDLESS approach in this case.

4.2. Computational savings

Next we demonstrate the saving in computational cost when using the non-adaptive version of ENDLESS to the standard approach (more saving can be expected when using the adaptive version). In the demonstration case, the number of CPU cores is fixed

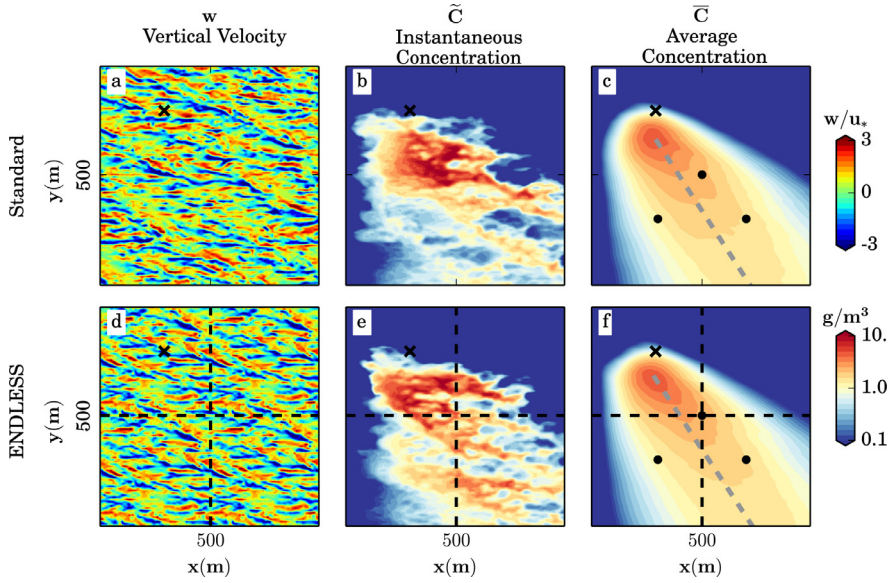

Fig. 5. Modeled Langmuir circulation and oil concentration field: The top row is the result from standard simulation and the bottom is the result from ENDLESS. (a, d) are vertical velocity at $z = -10$ m; (b, e) are instantaneous surface oil concentration and (c, f) are time-averaged surface concentration and their center lines (represented by grey dashed lines). The black cross symbol indicates the horizontal location of the oil source; the black dot symbols indicate the data sampling locations for Fig. 6.

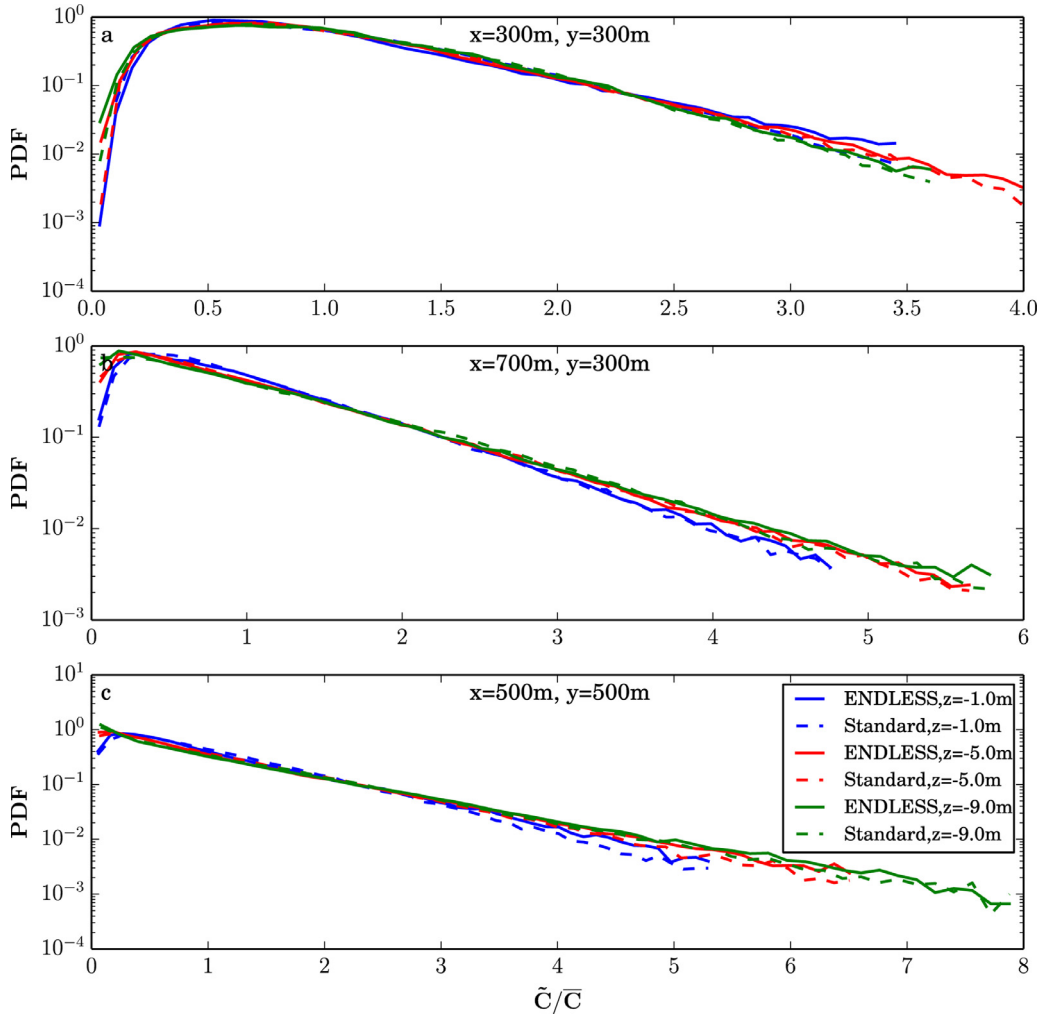

Fig. 6. Probability density functions of oil concentration at several locations and depths within the OML. The sampling area for each PDF corresponds to $100 \times 100\,m^2$ at each location, and the centers of sampling areas are shown as black dots in Fig. 5(c and f) The concentration is normalized by its local mean.

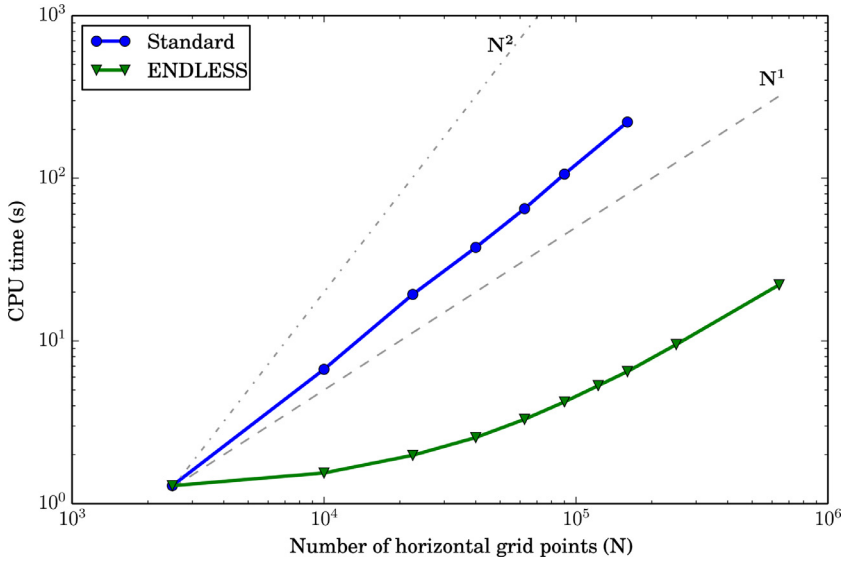

Fig. 7. Computational cost of standard and ENDLESS simulations. The ENDLESS simulations are all run in a "velocity-field LES domain" with 50 × 50 horizontal grid points. Grey lines indicate linear and quadratic increase of computational cost with number of horizontal grid points.

to be 15 and the number of grid points in the vertical direction is fixed to be 150. For the ENDLESS calculations, the number of horizontal grid points in the "velocity-field LES domain" is fixed at 50 × 50 and extended domains with square shape are chosen ($M_x = M_y = 1, 2, 3, \ldots$). For each extended domain size, the simulation is repeated for 5 times with 200 time-steps for each run to assemble robust average values for the consumed CPU time per time-step. Then the total computational cost is measured by the total consumed CPU time (i.e. the sum for all the 15 CPUs for each simulation). As shown in Fig. 7, the increase of total CPU time with the number of total horizontal grid points (N) for a benchmark case using standard LES is between linear and quadratic (slightly higher than the expected $N\log N$). When using ENDLESS to simulate the same physical problem, the total CPU time first increases very slowly for small N, and then increases almost linearly with N when the number of horizontal grid points exceeds about $N = 10^5$. Comparison between standard LES and ENDLESS shows that the latter achieves significant saving in computational cost for cases with very large total effective domain size for the plume simulation, which is crucial for tracking long-term transport and dilution of effluents.

4.3. Adaptive simulation with 2D large-scale eddies

The third and fourth simulations are set up with the inclusion of the adaptive extended domain and large-scale advection techniques to illustrate the application of the ENDLESS approach to oil transport. In this context, $\mathbf{U}_{LS}$ is used to represent the effect of submeso- and mesoscale eddies on oil transport. Submesoscale eddies have lateral scale of order 1 km, and are typically produced by baroclinic instabilities associated with horizontal density gradients (Thomas et al., 2008). Of importance here is the fact that these motions tend to be nearly two dimensional, quasi-geostrophic and hydrostatic (Hamlington et al., 2014), with vertical velocities significantly smaller than the ones in Langmuir cells and evolving much more slowly in time.

In real applications, the velocity field $\mathbf{U}_{LS}$ could be obtained from a numerical simulation of ocean circulations on a coarser grid, such as those produced by regional models. In the present illustrative application, for simplicity we use a "synthetic surrogate" velocity field that can be specified analytically. We use a two-mode cellular flow (with modes denoted by A and B in the expressions below) as a simplified proxy for submesoscale eddies. In particular, $\mathbf{U}_{LS} = (U_{LS}, V_{LS}, 0)$ extending in the entire vertical depth is given by:

$$\begin{cases} U_{LS} = U_A \sin\left(k_A x - \omega_{x,A} t + \phi_x\right) \cos\left(k_A y - \omega_{y,A} t + \phi_y\right) \\ \quad + U_B \sin\left(k_B x - \omega_{x,B} t\right) \cos\left(k_B y - \omega_{y,B} t\right), \\ V_{LS} = -U_A \cos\left(k_A x - \omega_{x,A} t + \phi_x\right) \sin\left(k_A y - \omega_{y,A} t + \phi_y\right) \\ \quad - U_B \cos\left(k_B x - \omega_{x,B} t\right) \sin\left(k_B y - \omega_{y,B} t\right), \end{cases} \tag{8}$$

where U_{LS} and V_{LS} are the large-scale velocity components in the x and y directions respectively. In this idealized flow field, the first cellular flow mode has maximum speed U_A, wavenumber $k_A = 2\pi/L_A$ (L_A is the wavelength), angular frequency with components $\omega_{x,A}$ and $\omega_{y,A}$, and phase shifts ϕ_x and ϕ_y in x and y directions, respectively. Similar parameters with subscript B are used for the second mode, which does not include phase shifts.

For the two demonstration simulations in this subsection only one stationary cellular flow mode is used ($U_B = 0$, $\omega_{x,A} = \omega_{y,A} = 0$, and $\phi_x = \phi_y = 0$). Its amplitude is set to $U_A = 6u_*$, which is approximately half of the mean surface Lagrangian velocity, and $L_A = 2$ km, corresponding to 2D eddies with a diameter of 1 km and Rossby number Ro = 1.07.

Two simulations with oil droplet diameters of 250 and 500 μm are carried out with the same flow field configuration to demonstrate the capability of ENDLESS for tracking the evolution of plumes with different characteristics. The oil source is turned on to release oil continuously for about 9 hours in the third simulation and 6 hours in the fourth, and then turned off to let the oil plume be transported and diluted by the flow. After the source is turned off, the 2D large-scale flow effect $\mathbf{U}_{LS}$ is initiated. Unlike the first two simulations used for validation in which the large-scale domain was held fixed and an outflow boundary condition was used for the scalar, in these two latter simulations since the plumes continually evolve, the total extended domain adaptively grows and migrates.

Figs. 8 and 9 show snapshots of the surface oil plume from the simulations with the 2D cellular flow for oil droplet diameters of 250 and 500 μm, respectively. Both the small-scale fingered structure of the surface oil plume caused by Langmuir circulations and the large-scale distortions caused by the cellular flow are visible in the figures. The squares with color contours represent "active" domains with scalar simulation at the chosen time-step.

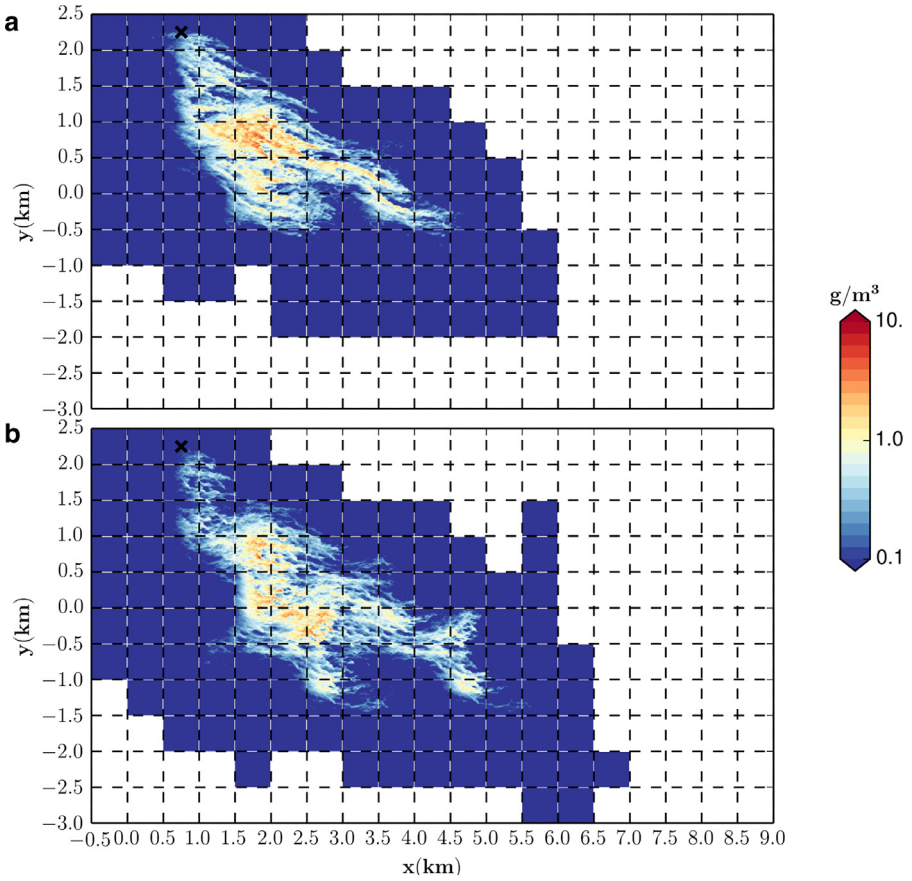

Fig. 8. Surface oil concentration dispersed in an adaptive extended domain coupled with a 2D cellular flow. The diameter of oil droplets is $d = 250\,\mu$m; Snapshots are shown for $t = 6$ h (a) and $t = 9$ h (b) after oil source is deactivated.

The adaptive evolution of the extended domain for scalar can be clearly seen by comparing the snapshots at different simulation times. In the present case, the evolution of the domain also illustrates physical differences in the transport of droplets with different sizes. The smaller oil droplets have smaller rise velocity (Fig. 8) and are transported deeper into the OML by the strong downwelling velocities associated with the Langmuir cells. Thus a plume of smaller droplets occupies most of the OML depth, experiencing more horizontal spreading and resulting in a larger surface plume (note that the mean velocity direction changes with depth due to the Ekman spiral and the Stokes drift.). Therefore, the adaptive extended domain expands significantly as time evolves (Figs. 8a and b). Differently, the larger droplets have large enough rise velocity to overcome the downwelling effect and stay on the surface (Fig. 9), being transported mainly by the mean surface velocity. Thus, the oil plume with large droplets is transported downstream with smaller lateral dispersion. Consequently, the adaptive extended domain follows the migration of the oil plume, with less significant expansion compared to the smaller droplet case. Using ENDLESS, the multiscale characteristics of these distinct oil plumes can be well captured.

As a rough estimate of the computational cost saving associated with the domain adaptivity, if one is interested in tracking the plume in a 10 x 10 km domain using the setup in Figs. 8 and 9, the computational cost of ENDLESS without adaptivity would be proportional to the total number of domains (i.e. 400 domains of 500 × 500 m), while computation with domain adaptivity only requires about 110 domains for the small droplet case (Fig. 8b) and 80 domains for the large droplet case (Fig. 9). Thus, for this model configuration, a saving in computational cost between 72% and 80% is achieved by including adaptivity. This calculation does not take into account the additional gain in the initial period of the simulation, when only very few domains are required if domain adaptivity is included.

4.4. Effects of Langmuir circulations

An important question for oil plume dispersion that can be addressed with ENDLESS is how different types of 3D turbulence may affect the overall transport and plume properties when subjected to the same large-scale velocity field. We consider turbulence with and without Langmuir circulations. Two simulations are performed with the same setup except that in the first simulation the Stokes drift velocity is included and in the second one it is set to zero (thus eliminating the formation of Langmuir cells and their modulation of turbulence in the LES portion of ENDLESS).

For the large-scale velocity field, the two-mode cellular flow is used, with wavelengths $L_A = 2.0$ km and $L_B = 5.6$ km corresponding to eddies with diameters of 1.0 and 2.8 km. The mode amplitudes are set to $U_A = U_B = 2u_*$, yielding Rossby numbers equal to 0.35 and 0.12, respectively. The phase difference between the cellular flows is set to $\phi_x = 0.3\pi$ and $\phi_y = -0.5\pi$. Finally, the angular frequencies are chosen so that the cellular flow pattern moves with the mean Lagrangian velocity at the ocean surface (U^L_{sfc}, V^L_{sfc}), where the mean Lagrangian velocity is defined as $(\langle\overline{u}\rangle + U_s, \langle\overline{v}\rangle)$ (i.e. $\omega_{x,A} = U^L_{sfc}k_A$ and $\omega_{y,A} = V^L_{sfc}k_A$ and similarly for B).

In both simulations with and without Stokes drift, a continuous oil source is used and droplet sizes are set to 500 μm. Snapshots of the two simulations are shown in Fig. 10. Note, that except for the Lagrangian velocity (which is impacted by the Stokes drift), the large-scale flow features are the same for both simulations. As expected, the presence of Langmuir circulations produces

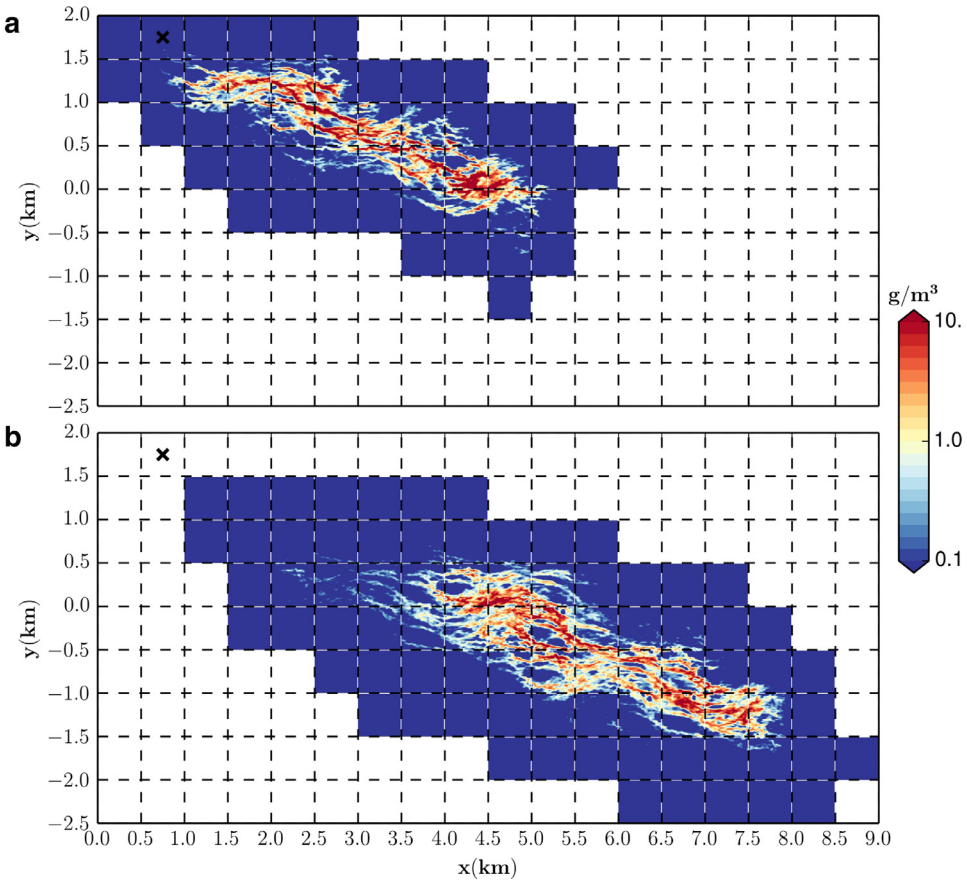

Fig. 9. Same as Fig. 8 except for $d = 500\,\mu$m.

"fingered" oil plumes with high oil concentrations in the surface convergence zones corresponding to the downwelling branches of the Langmuir cells (Yang et al., 2014; 2015). More interestingly, the presence of Langmuir cells strongly impacts the response of the oil plume to the large-scale flow. The stronger turbulence in the Langmuir case enhances the initial horizontal plume spread. Thus, the plume quickly reaches widths comparable to the scale of the submesoscale eddies, which in turn contribute to increasing the horizontal spread of the oil. Conversely, in the case without Langmuir cells, the initial plume spread is reduced, and the main effect of the 2D eddies is to produce a meandering of the plume as a whole, with significantly less dilution.

As a final note, in this case of a continuous oil release, the computational gain is not as large because the adaptive domain is pinned at the source and grows downstream with the growing plume. In the snapshots depicted in Fig. 10, the saving in computational cost from adaptivity is around 59% without Stokes drift and 52% with Stokes drift, as computational cost is estimated by the fraction of the grey area over the minimum rectangular area which encloses this grey area.

5. Conclusions

In this work, we describe a new approach, the Extended Nonperiodic Domain LES for Scalar plume (ENDLESS), to study the transport and dispersion of passive scalars over a large domain using LES.

ENDLESS consists of three main components: (i) replication of the small-scale turbulence velocity domain to advect a passive scalar plume on a larger domain (as in Matheou and Bowman (2015), leveraging the periodic boundary conditions of the velocity and pressure fields to adaptively extend the scalar domain without extending the "velocity-field LES domain" directly), (ii) an adaptive-domain technique used to dynamically track the nonhomogeneous scalar plume with minimum computational cost, and (iii) assumption of scale-separation to include the advection of the passive scalar by large-scale flow features such as submeso- and mesoscale eddies.

A comparison study is performed to demonstrate that ENDLESS yields similar results compared to LES when the latter is implemented on the extended domain. The results show that periodic repetition is a promising approach to simulate scalar plumes on large domains. ENDLESS is also shown to have a much lower computational cost compared to the standard approach of directly simulating all the scales of interest. Also, in this paper, an idealized 2D cellular flow field that can be prescribed analytically is used to demonstrate the coupling technique.

In practice, we envision the coupling of ENDLESS with a regional circulation models such as HYCOM. In such a two-model approach ENDLESS is used as a "local downscaling" tool to study oil plumes within subregions of interest where one wishes to describe advection of oil with more spatial detail than what is available from the regional ocean models. In our view, this represents important gains in accuracy compared to the current approach of using only a regional model and relying on KPP or some alternative closure approach to represent the complex effects of Langmuir turbulence on the oil transport within the ocean mixed layer. Of course, at the current stage, the coupling between the two modeling approaches occurs only in the oil advection, but this is certainly already a great improvement over the current approach. Needless to say, ENDLESS should not be seen as a replacement of fully (two-way) coupled simulations of the full multiscale

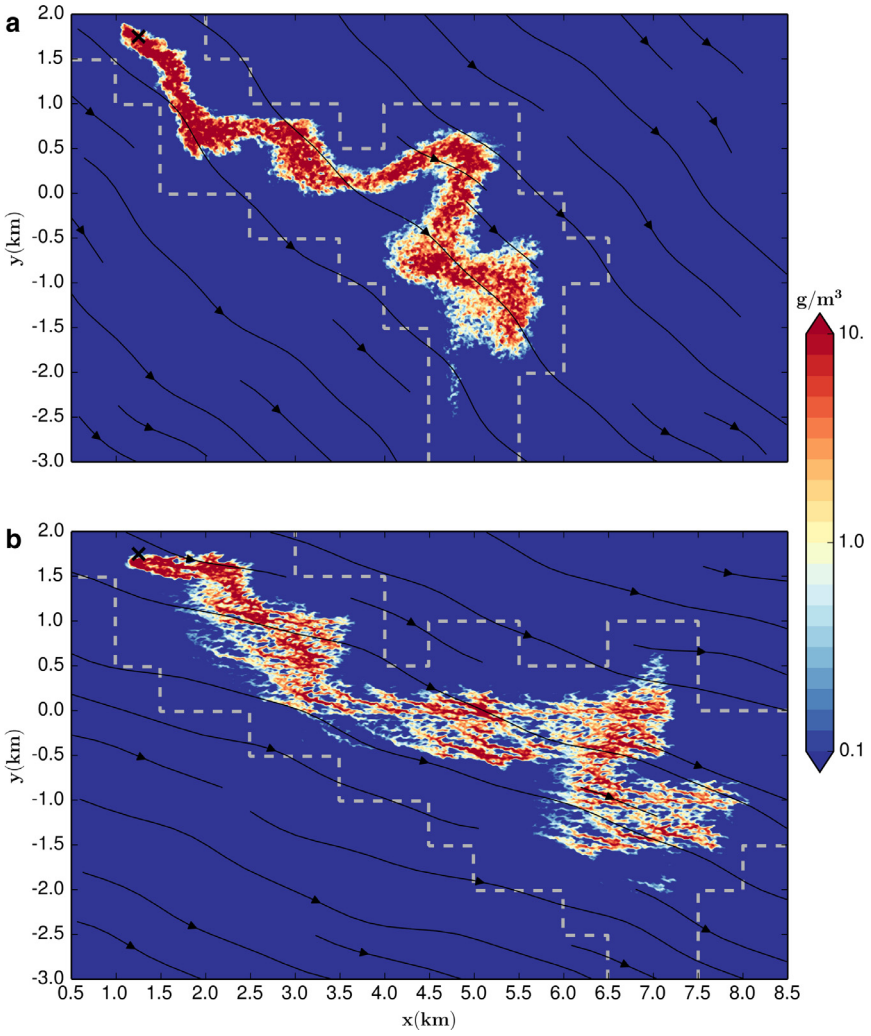

Fig. 10. Surface oil concentration dispersed in an adaptive extended domain coupled with a 2D cellular flow. The diameter of oil droplets is $d = 500\,\mu$m; Snapshots are shown for (a) case without Langmuir circulations and (b) case including Langmuir circulations. Black lines indicate the streamlines formed by the superposition of the mean flow from the LES and the 2D eddies. Grey dashed lines indicate the "active" ENDLESS domain at the moment of the snapshots.

Navier-Stokes dynamics. However such fully coupled approaches are often prohibitive and ENDLESS can provide a more affordable approach in practice.

Acknowledgements

This research was made possible by a grant from The Gulf of Mexico Research Initiative. Data are publicly available through the Gulf of Mexico Research Initiative Information & Data Cooperative (GRIIDC) at https://data.gulfresearchinitiative.org (doi:10.7266/N7ST7MTP). We are grateful to Prof. Lian Shen for useful suggestions and comments on this work.

References

Belcher, S.E., Grant, A.L., Hanley, K.E., Fox-Kemper, B., Van Roekel, L., Sullivan, P.P., Large, W.G., Brown, A., Hines, A., Calvert, D., et al., 2012. A global perspective on Langmuir turbulence in the ocean surface boundary layer. Geophys. Res. Lett. 39.

Bou-Zeid, E., Meneveau, C., Parlange, M., 2005. A scale-dependent lagrangian dynamic model for large eddy simulation of complex turbulent flows. Phys. Fluids (1994-present) 17. http://scitation.aip.org/content/aip/journal/pof2/17/2/10.1063/1.1839152.

Chamecki, M., Meneveau, C., Parlange, M.B., 2008. A hybrid spectral/finite-volume algorithm for large-eddy simulation of scalars in the atmospheric boundary layer. Bound.-Lay. Meteorol. 128, 473–484.

Chamecki, M., Meneveau, C., Parlange, M.B., 2009. Large eddy simulation of pollen transport in the atmospheric boundary layer. J. Aerosol Sci. 40, 241–255. doi:10.1016/j.jaerosci.2008.11.004. http://www.sciencedirect.com/science/article/pii/S0021850208002024.

Craik, A.D.D., 1977. The generation of Langmuir circulations by an instability mechanism. J. Fluid Mech. 81, 209–223. http://journals.cambridge.org/article_S0022112077001980.

Craik, A.D.D., Leibovich, S., 1976. A rational model for Langmuir circulations. J. Fluid Mech. 73, 401–426. http://journals.cambridge.org/article_S0022112076001420.

Ferry, J., Balachandar, S., 2001. A fast eulerian method for disperse two-phase flow. Int. J. Multiphase Flow 27, 1199–1226. http://www.sciencedirect.com/science/article/pii/S0301932200000690.

Gaskell, P.H., Lau, A.K.C., 1988. Curvature-compensated convective transport: smart, a new boundedness- preserving transport algorithm. Int. J. Numer. Meth. Fluids 8, 617–641. http://dx.doi.org/10.1002/fld.1650080602.

Grant, A.L., Belcher, S.E., 2009. Characteristics of Langmuir turbulence in the ocean mixed layer. J. Phys. Oceanogr. 39.

Hamlington, P.E., Van Roekel, L.P., Fox-Kemper, B., Julien, K., Chini, G.P., 2014. Langmuir–submesoscale interactions: descriptive analysis of multiscale frontal spin-down simulations. J. Phys. Oceanogr. 44, 2249–2272.

Henn, D., Sykes, R., 1992. Large-eddy simulation of dispersion in the convective boundary layer. Atmos. Environ. Part A. Gen. Top. 26, 3145–3159.

Huntley, H.S., Lipphardt, B.L., Kirwan, A.D., 2013. Surface drift predictions of the deepwater horizon spill: the Lagrangian perspective. Am. Geophys. Union, pp. 179–195. http://dx.doi.org/10.1029/2011GM001097.

Imberger, J., 2013. Environmental Fluid Dynamics: Flow Processes, Scaling, Equations of Motion, and Solutions to Environmental Flows. Academic Press.

Langmuir, I., 1938. Surface motion of water induced by wind. Science 87, 119–123.

Large, W.G., McWilliams, J.C., Doney, S.C., 1994. Oceanic vertical mixing: a review and a model with a nonlocal boundary layer parameterization. Rev. Geophys. 32, 363–403.

Le Henaff, M., Kourafalou, V.H., Paris, C.B., Helgers, J., Aman, Z.M., Hogan, P.J., Srinivasan, A., 2012. Surface evolution of the deepwater horizon oil spill patch: combined effects of circulation and wind-induced drift. Env. Sci. Technol. 46, 7267–7273. doi:10.1021/es301570w. PMID: 22676453.

Leibovich, S., 1977. Convective instability of stably stratified water in the ocean. J. Fluid Mech. 82, 561–581. http://journals.cambridge.org/article_S0022112077000846.

Leibovich, S., 1977. On the evolution of the system of wind drift currents and Langmuir circulations in the ocean. Part 1. theory and averaged current. J. Fluid Mech. 79, 715–743. http://journals.cambridge.org/article_S002211207700041X.

Leibovich, S., 1983. The form and dynamics of Langmuir circulations. Annu. Rev. Fluid Mech. 15, 391–427.

Matheou, G., Bowman, K., 2015. A recycling method for the large-eddy simulation of plumes in the atmospheric boundary layer. Environ. Fluid Mech. 1–17. http://dx.doi.org/10.1007/s10652-015-9413-4.

McWilliams, J.C., Huckle, E., Liang, J., Sullivan, P.P., 2014. Langmuir turbulence in swell. J. Phys. Oceanogr. 44, 870–890.

McWilliams, J.C., Sullivan, P.P., 2000. Vertical mixing by Langmuir circulations. Spill Sci. Technol. Bull. 6, 225–237.Langmuir Circulation and Oil Spill Modeling

McWilliams, J.C., Sullivan, P.P., Moeng, C.H., 1997. Langmuir turbulence in the ocean. J. Fluid Mech. 334, 1–30. http://journals.cambridge.org/article_S0022112096004375.

Moeng, C.H., 1984. A large-eddy-simulation model for the study of planetary boundary-layer turbulence. J. Atmos. Sci. 41, 2052–2062.

Moin, P., Kim, J., 1982. Numerical investigation of turbulent channel flow. J. Fluid Mech. 118, 341–377.

Özgökmen, T.M., Poje, A.C., Fischer, P.F., Childs, H., Krishnan, H., Garth, C., Haza, A.C., Ryan, E., 2012. On multi-scale dispersion under the influence of surface mixed layer instabilities and deep flows. Ocean Modell. 56, 16–30.

Özgökmen, T.M., Poje, A.C., Fischer, P.F., Haza, A.C., 2011. Large eddy simulations of mixed layer instabilities and sampling strategies. Ocean Modell. 39, 311–331.

Poje, A.C., Özgökmen, T.M., Lipphardt, B.L., Haus, B.K., Ryan, E.H., Haza, A.C., Jacobs, G.A., Reniers, A., Olascoaga, M.J., Novelli, G., et al., 2014. Submesoscale dispersion in the vicinity of the deepwater horizon spill. Proc. Natl. Acad, Sci. 111, 12693–12698.

Scotti, A., 2010. Large eddy simulation in the ocean. Int. J. Comput. Fluid Dyn. 24, 393–406. http://dx.doi.org/10.1080/10618562.2010.522527.

Smyth, W.D., Skyllingstad, E.D., Crawford, G.B., Wijesekera, H., 2002. Nonlocal fluxes and stokes drift effects in the k-profile parameterization. Ocean Dyn. 52, 104–115.

Sullivan, P.P., McWilliams, J.C., 2010. Dynamics of winds and currents coupled to surface waves. Annu. Rev. Fluid Mech. 42, 19–42. http://dx.doi.org/10.1146/annurev-fluid-121108-145541.

Sullivan, P.P., Patton, E.G., 2011. The effect of mesh resolution on convective boundary layer statistics and structures generated by large-eddy simulation. J. Atmos. Sci. 2395–2415.

Sullivan, P.P., Romero, L., McWilliams, J.C., Melville, W.K., 2012. Transient evolution of Langmuir turbulence in ocean boundary layers driven by hurricane winds and waves. J. Phys. Oceanogr. 42, 1959–1980.

Thomas, L.N., Tandon, A., Mahadevan, A., 2008. Submesoscale processes and dynamics. Ocean Model. Eddying Regime, Geophys. Monogr. Ser 177, 17–38.

Thorpe, S., 2004. Langmuir circulation. Annu. Rev. Fluid Mech. 36, 55–79. http://dx.doi.org/10.1146/annurev.fluid.36.052203.071431.

Tseng, Y.H., Meneveau, C., Parlange, M.B., 2006. Modeling flow around bluff bodies and predicting urban dispersion using large eddy simulation. Env. Sci. Technol. 40, 2653–2662.

Van Roekel, L., Fox-Kemper, B., Sullivan, P., Hamlington, P., Haney, S., 2012. The form and orientation of Langmuir cells for misaligned winds and waves. J. Geophys. Res.: Oceans (1978–2012) 117.

Yang, D., Chamecki, M., Meneveau, C., 2014. Inhibition of oil plume dilution in Langmuir ocean circulation. Geophys. Res. Lett. 41, 1632–1638. http://dx.doi.org/10.1002/2014GL059284.

Yang, D., Chen, B., Chamecki, M., Meneveau, C., 2015. Oil plumes and dispersion in Langmuir, upper-ocean turbulence: large-eddy simulations and k-profile parameterization. J. Geophys. Res. – Oceans doi:10.1002/2014JC010542.